

# Gamma-ray spectra from thermal neutron capture on gadolinium-155 and natural gadolinium

Tomoyuki Tanaka<sup>1</sup>, Kaito Hagiwara<sup>1</sup>, Enrico Gazzola<sup>3</sup>, Ajmi Ali<sup>1,6,\*</sup>, Iwa Ou<sup>1</sup>, Takashi Sudo<sup>1,8</sup>, Pretam Kumar Das<sup>1,9</sup>, Mandeep Singh Reen<sup>1,10</sup>, Rohit Dhir<sup>1,11</sup>, Yusuke Koshio<sup>1</sup>, Makoto Sakuda<sup>1,\*</sup>, Atsushi Kimura<sup>2</sup>, Shoji Nakamura<sup>2</sup>, Nobuyuki Iwamoto<sup>2</sup>, Hideo Harada<sup>2</sup>, Gianmaria Collazuol<sup>3</sup>, Sebastian Lorenz<sup>4</sup>, Michael Wurm<sup>4</sup>, William Focillon<sup>5</sup>, Michel Gonin<sup>5</sup>, and Takatomi Yano<sup>7</sup>

<sup>1</sup>Department of Physics, Okayama University, Okayama 700-8530, Japan

<sup>2</sup>Japan Atomic Energy Agency, 2-4 Shirakata Shirane, Tokai, Naka, Ibaraki 319-1195, Japan

<sup>3</sup>Università di Padova and INFN, Dipartimento di Fisica, Padova 35131, Italy

<sup>4</sup>Institut für Physik, Johannes Gutenberg-Universität Mainz, 55128 Mainz, Germany

<sup>5</sup>Département de Physique, École Polytechnique, 91128 Palaiseau Cedex, France

<sup>6</sup>Present address: Department of Physics, Kyoto University, Kyoto 606-8502, Japan

<sup>7</sup>Present address: Kamioka Observatory, ICRR, University of Tokyo, Gifu 506-1205, Japan

<sup>8</sup>Present address: Research Center for Nuclear Physics (RCNP), Osaka University, Osaka 567-0047, Japan

<sup>9</sup>Present address: Department of Physics, Pabna University of Science & Technology, Pabna-6600, Bangladesh

<sup>10</sup>Present Address: Department of Physics, Akal University, Punjab 151302, India

<sup>11</sup>Present address: Research Institute & Department of Physics and Nano Technology, SRM University, Kattankulathur-603203, India

\*E-mail: ali.ajmi.3c@kyoto-u.ac.jp, sakuda-m@okayama-u.ac.jp

Received July 10, 2019; Revised January 26, 2020; Accepted January 30, 2020; Published April 13, 2020

.....  
 Natural gadolinium is widely used for its excellent thermal neutron capture cross section, because of its two major isotopes: <sup>155</sup>Gd and <sup>157</sup>Gd. We measured the  $\gamma$ -ray spectra produced from the thermal neutron capture on targets comprising a natural gadolinium film and enriched <sup>155</sup>Gd (in Gd<sub>2</sub>O<sub>3</sub> powder) in the energy range from 0.11 MeV to 8.0 MeV, using the ANNRI germanium spectrometer at MLF, J-PARC. The freshly analyzed data of the <sup>155</sup>Gd(*n*,  $\gamma$ ) reaction are used to improve our previously developed model (ANNRI-Gd model) for the <sup>157</sup>Gd(*n*,  $\gamma$ ) reaction [K. Hagiwara et al. [ANNRI-Gd Collaboration], Prog. Theor. Exp. Phys. **2019**, 023D01 (2019)], and its performance confirmed with the independent data from the <sup>nat</sup>Gd(*n*,  $\gamma$ ) reaction. This article completes the development of an efficient Monte Carlo model required to simulate and analyze particle interactions involving the thermal neutron captures on gadolinium in any relevant future experiments.  
 .....

Subject Index C42, C43, D21, F20, F22, H20, H43

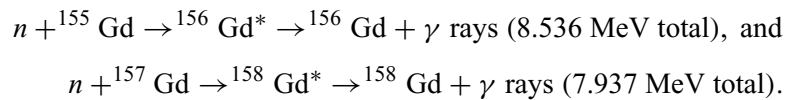
## 1. Introduction

Gadolinium (Gd) has become an important element of consideration in a number of neutrino experiments for enhanced detection of electron anti-neutrinos ( $\bar{\nu}_e$ ). The presence of Gd boosts the tagging of neutrons in the inverse beta decay reaction (IBD),  $\bar{\nu}_e + p \rightarrow e^+ + n$ , in organic liquid scintillator and water-Cherenkov detectors. This is primarily due to its large capture cross

**Table 1.** Relative abundances of gadolinium isotopes in natural gadolinium [20] and their radiative thermal neutron capture cross sections [1].

Isotope	Abundance [%]	Cross section [b]
$^{152}\text{Gd}$	0.200	735
$^{154}\text{Gd}$	2.18	85
<b><math>^{155}\text{Gd}</math></b>	<b>14.80</b>	<b>60 900</b>
$^{156}\text{Gd}$	20.47	1.8
<b><math>^{157}\text{Gd}</math></b>	<b>15.65</b>	<b>254 000</b>
$^{158}\text{Gd}$	24.84	2.2
$^{160}\text{Gd}$	21.86	1.4

section for thermal neutrons and the large energy released by  $\gamma$  rays of  $\sim 8$  MeV for the  $\text{Gd}(n, \gamma)$  reactions [1–4]:



The element has already been used as a neutron absorber in scintillator-based detectors for the neutrino oscillation experiments [5–13] and a neutrino-flux monitor experiment [14]. For the upcoming SuperKamiokande-Gd (SK-Gd) phase [15–17], Gd will be dissolved in a multi-kiloton water-Cherenkov detector. The application of Gd-loaded detector materials for neutron tagging is foreseen for direct dark matter search experiments like LZ [18] and XENONnT [19].

Therefore, it is of paramount importance to establish a precise Monte Carlo (MC) model for the  $\gamma$ -ray energy spectrum from the radiative thermal neutron capture on Gd. It is an essential prerequisite for MC studies aiming to evaluate the neutron tagging efficiency in a Gd-loaded detector. Precise modeling is especially important for those detectors that lack hermetic acceptance and/or have a high energy threshold for  $\gamma$  rays, since some of the  $\gamma$  rays emitted in the capture reaction may not be detected.

In most cases, detector materials are doped with the natural Gd ( ${}^{\text{nat}}\text{Gd}$ ). Isotopic abundances are listed in Table 1.

The most frequent isotopes,  $^{155}\text{Gd}$  and  $^{157}\text{Gd}$ , also feature large thermal neutron capture cross sections. Therefore, the required MC model for  ${}^{\text{nat}}\text{Gd}$  requires the modeling of the  $\gamma$ -ray emission from not only  $^{157}\text{Gd}$  [21] but also  $^{155}\text{Gd}$ .

We measured the  $\gamma$ -ray energy spectrum from the radiative thermal neutron capture on an enriched  $^{155}\text{Gd}$  sample and a  ${}^{\text{nat}}\text{Gd}$  film with the germanium (Ge) spectrometer of the Accurate Neutron–Nucleus Reaction Measurement Instrument (ANNRI) [22–26]. The incident pulsed neutron beam from the Japan Spallation Neutron Source (JSNS) at the Material and Life Science Experimental Facility (MLF) of the Japan Proton Accelerator Research Complex (J-PARC) [27] and the good  $\gamma$ -ray energy resolution, high statistics, and low background makes ANNRI a favorable spectrometer for our intended study [21,22].

The Detector for Advanced Neutron Capture Experiments (DANCE) at the Los Alamos Neutron Science Center (LANSCE) has extensively studied the  $\gamma$ -ray energy spectra from the radiative neutron capture reaction at various multiplicities in the neutron kinetic energy range from 1 to 300 eV for both  $^{155}\text{Gd}$  and  $^{157}\text{Gd}$  targets [28–30]. They compared their  $\gamma$ -ray spectra to MC simulations with the DICEBOX package [31] and showed fair agreement. Concerning the measurements in the

thermal energy region, Groshev et al. [32–34] measured prompt  $\gamma$  rays from the neutron capture on  $^{155}\text{Gd}$  and  $^{157}\text{Gd}$  and tabulated the  $\gamma$ -ray energy, intensity values and decay schemes in great detail. Valenta et al. [35] measured the two-step cascade (TSC)  $\gamma$  rays, following the thermal neutron capture on  $^{155}\text{Gd}$  and  $^{157}\text{Gd}$ , with a pair of HPGe detectors and studied the effect of the  $M1$  or  $E2$  transitions in addition to the  $E1$  transitions in the TSC spectra.

We performed a series of measurements of the prompt  $\gamma$  rays covering almost the full spectrum from 0.11 MeV to 9 MeV from the capture reaction on  $^{155,157}\text{Gd}$  and  $^{\text{nat}}\text{Gd}$  at thermal neutron energies. As we demonstrated in Fig. 12 of the previous publication [21] and also Fig. 7 of this report, it is very important to measure the full  $\gamma$ -ray spectrum from the capture in order to study the photon strength function and the nuclear level density, which are the important properties of the Gd nucleus<sup>1</sup>. Based on our data and a Geant4-based detector simulation [36,37] of our setup, we developed a Monte Carlo (MC) model to generate the full  $\gamma$ -ray spectrum from the thermal  $^{157,155,\text{nat}}\text{Gd}(n,\gamma)$  reaction. The  $\gamma$ -ray spectrum and its corresponding MC model (ANNRI-Gd model) for  $^{157}\text{Gd}$  has already been discussed in Ref. [21].

In this report, we present the  $\gamma$ -ray energy spectra from the  $^{155}\text{Gd}(n,\gamma)$  and  $^{\text{nat}}\text{Gd}(n,\gamma)$  reactions, modify our ANNRI-Gd model with the contribution from  $^{155}\text{Gd}$ , and present our final MC performance for  $^{\text{nat}}\text{Gd}(n,\gamma)$  to be used by any neutrino or other experiments involving the measurement of  $\gamma$ -ray signals from the thermal neutron capture on Gd.

## 2. Experiment and data analysis

A 300 kW beam of 3 GeV protons from the JSNS facility in double-bunch mode at a frequency of 25 Hz was incident on a primary target of mercury, producing neutrons. The neutron beam thus produced consists of neutron pulses in double-bunch mode, each 100 ns wide, with 600 ns spacing every 40 ms. The ANNRI spectrometer is located 21.5 m away from the neutron beam source. It comprises two germanium cluster detectors with anti-coincidence shields made of bismuth germanium oxide (BGO) and eight co-axial germanium detectors. The target for neutron capture is positioned in line with the beam, 13.4 cm from each of the two cluster detectors on either side along the vertical plane.

In this report, we used only data taken with the cluster detectors, which cover 15% of the solid angle. Each cluster consists of seven Ge crystals in a hexagonal arrangement, details of which can be found in Ref. [21].

From the neutron time-of-flight  $T_{\text{TOF}}$  recorded for each event we calculated the neutron kinetic energy  $E_n$  as

$$E_n = m_n(L/T_{\text{TOF}})^2/2, \quad (1)$$

where  $m_n$  is the neutron mass and  $L$  is the 21.5 m distance between neutron source and target. The resulting neutron energy spectra are shown in Fig. 1. Since we study the  $\gamma$ -ray spectrum solely from thermal neutron capture on  $^{155}\text{Gd}$  and  $^{\text{nat}}\text{Gd}$ , we only selected events from neutrons in the kinetic energy range [4, 100] meV for the present analysis.

The obtained data cover the energy region of  $\gamma$  rays from 0.11 MeV to about 9 MeV with observed  $\gamma$ -ray multiplicities ( $M$ ) one to three. The energies of the emitted  $\gamma$  rays are recorded by each of the

<sup>1</sup> The high-energy part of the  $\gamma$ -ray spectrum above 4 MeV is dominated by the first  $\gamma$ -ray transition from the resonance and is sensitive to the shape of the  $E1$  photon strength function; the low-energy part of the spectrum below 4 MeV is mainly contributed to by the subsequent cascade  $\gamma$  rays.

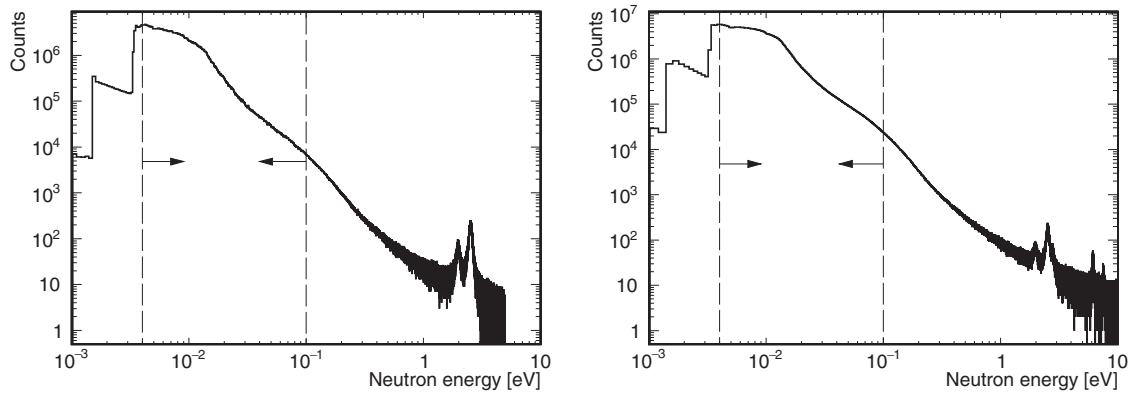


**Fig. 1.** Energy spectrum of neutrons as obtained with the observed neutron time-of-flight according to Eq. (1) for the  $^{155}\text{Gd}$  target (left) and the  $^{\text{nat}}\text{Gd}$  target (right).

**Table 2.** Isotopic compositions of the  $\text{Gd}_2\text{O}_3$  targets.

Isotope	$^{152}\text{Gd}$	$^{154}\text{Gd}$	$^{155}\text{Gd}$	$^{156}\text{Gd}$	$^{157}\text{Gd}$	$^{158}\text{Gd}$	$^{160}\text{Gd}$
$^{155}\text{Gd}_2\text{O}_3$	<0.02	0.5	91.9( $\pm$ 0.3)	5.87	0.81	0.65	0.27
$^{157}\text{Gd}_2\text{O}_3$	<0.01	0.05	0.3	1.63	88.4( $\pm$ 0.2)	9.02	0.6

crystals. A threshold of 100 keV is set for each of the cluster detectors. For the event classification, we assign a multiplicity value  $M$  and a hit value  $H$  to each recorded event. We defined the multiplicity  $M$  as the combined number of isolated sub-clusters of hit Ge crystals at the upper and lower clusters. A sub-cluster is formed by the neighboring hit Ge crystals and can be of size  $\geq 1$ . The hit value  $H$  describes the total number of Ge crystals hit in the event. The multiplicity  $M$  represents the number of observed  $\gamma$  rays, while the hit value  $H$  is a measure of the lateral spread of  $\gamma$  rays. The details of the event class are described in Ref. [21]. The fraction of the data collected in each event class is reflected in the bar charts in Fig. A.1.

We used radioactive sources ( $^{60}\text{Co}$ ,  $^{137}\text{Cs}$ , and  $^{152}\text{Eu}$ ) and  $^{35}\text{Cl}(n,\gamma)$  to calibrate the detector, and determined the detection efficiency of the spectrometer for  $\gamma$  rays at energies from 0.3 to 8.5 MeV, as described in detail in Ref. [21].

We measured the thermal neutron capture on a gadolinium ( $\text{Gd}_2\text{O}_3$ ) target enriched with  $^{155}\text{Gd}$  (91.85%) in December 2014 and natural Gd (99.9% pure metal film) in March 2013. The weights of the targets, i.e.,  $^{155}\text{Gd}$  and  $^{157}\text{Gd}$  powder, were 26.4 mg and 28.9 mg respectively, spread across an area of  $1 \times 1$  cm in a Teflon envelope. The film of the natural gadolinium target was  $5 \text{ mm} \times 5 \text{ mm} \times 10 \mu\text{m}$  (and  $20 \mu\text{m}$ ) in dimensions. The isotopic composition of our enriched gadolinium sample is given in Table 2.

In 2014, an additional layer of LiF ( $\sim 1$  cm thickness) was included in the beam pipe to reduce the  $\gamma$  rays from neutron capture on the aluminum of the beam pipe. Therefore, the data-taking with  $^{\text{nat}}\text{Gd}$  was subject to more background events (without the LiF layer) than that of  $^{155,157}\text{Gd}$ . The background  $\gamma$ -ray energy spectra that were observed by one of the crystals (C6) for M1H1 events (one  $\gamma$  and one hit) with the empty target holder at two different periods in the neutron beam are shown in Fig. 2. The  $\gamma$ -ray energy spectra for M1H1 events with the three target materials,  $^{155}\text{Gd}$ ,  $^{157}\text{Gd}$  (2014), and  $^{\text{nat}}\text{Gd}$  (2013), are also shown in Fig. 2. The histograms shown are normalized with reference to the livetime of the  $^{155}\text{Gd}$  data set. The differences in the observed count rates are due

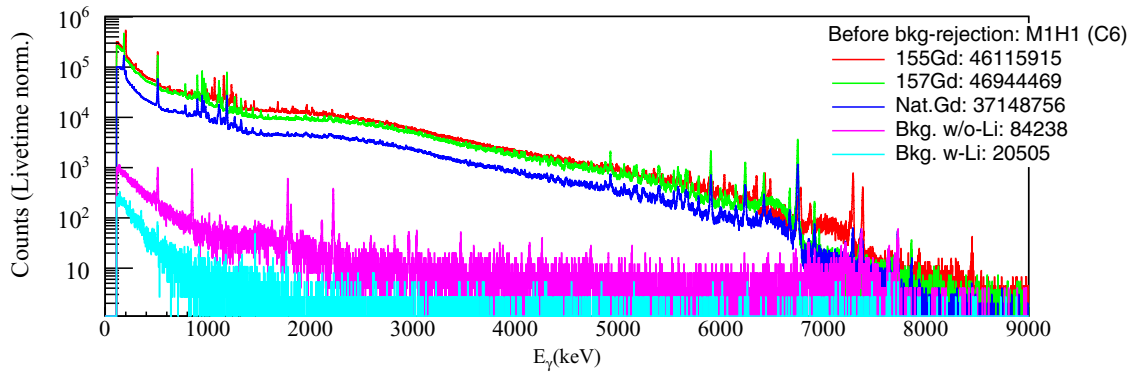


**Fig. 2.** Energy spectra for M1H1 (one  $\gamma$  and one hit) events obtained with neutron beam on the targets  $^{155}\text{Gd}$ ,  $^{157}\text{Gd}$ , and natural gadolinium, and the blank target holder as recorded in 2013 (w/o LiF) and 2014 (with LiF). The numbers show the data statistics in each case.

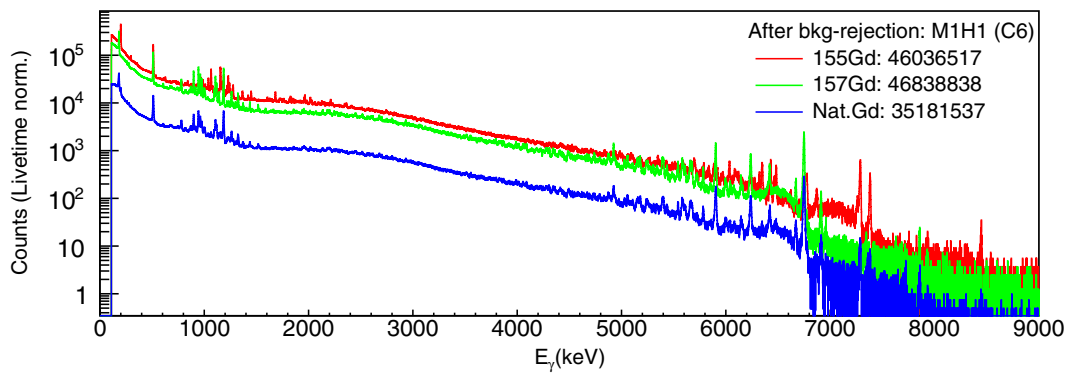


**Fig. 3.** Energy spectra for M1H1 events obtained with neutron beam on the targets  $^{155}\text{Gd}$ ,  $^{157}\text{Gd}$ , and natural gadolinium, after subtracting the background. The numbers show the data statistics in each case.

to the differences in the target masses ( $\times$  cross section) used for the three measurements. The size of the background is less than 0.1% for the data for the  $^{155}\text{Gd}$  target and less than 1% for those for the  $^{\text{nat}}\text{Gd}$  target. The background is accordingly subtracted for each data set and the resulting energy spectra for the three targets are shown in Fig. 3.

The  $\gamma$ -ray energy spectrum from neutron capture on natural gadolinium is dominated by that from its two main isotopes,  $^{155}\text{Gd}$  and  $^{157}\text{Gd}$ , with fractions of 18.5% and 81.5%, respectively. The contributions of other isotopes are negligible.

The spectra taken separately for the pure  $^{155}\text{Gd}$  and  $^{157}\text{Gd}$  samples must be consistent with that of the  $^{\text{nat}}\text{Gd}$  film, when they are combined in the corresponding proportions. This was checked and confirmed in Fig. 4, where excellent agreement is found between the two spectra (red and black).

### 3. Update for the ANNRI-Gd model

The MC model for  $^{157}\text{Gd}$  has already been described in Ref. [21]. We now develop a MC model for  $^{155}\text{Gd}$ , following the same approach of separate treatment for the discrete and continuum parts of the spectrum [21,38].

For the thermal neutron capture on  $^{155}\text{Gd}$  in an s-wave, the resonance state is 8.536 MeV ( $J^\pi = 2^-$ ) of  $^{156}\text{Gd}$ . The resonance energy for the neutron is  $26.8 \pm 0.2$  meV and the radiative width is  $108 \pm 1$  meV [1]. We identified and measured the photo peak intensities of 12 discrete  $\gamma$  rays for  $^{155}\text{Gd}(n, \gamma)$

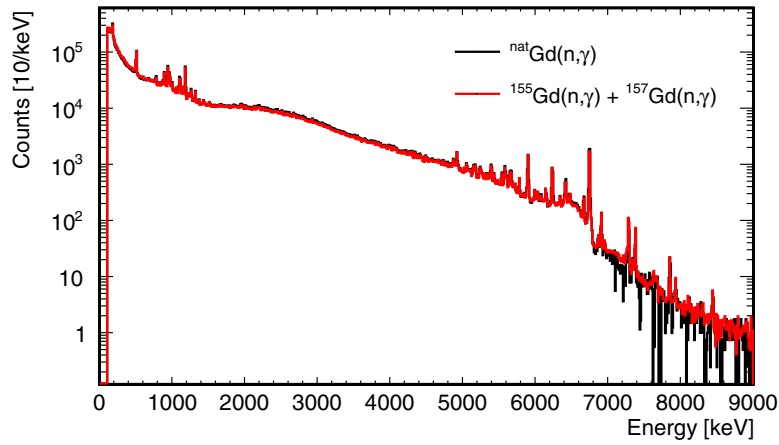


**Fig. 4.** Comparison of the combined energy spectra of  $^{155}\text{Gd}$  and  $^{157}\text{Gd}$  (red) with that of natural gadolinium (black).

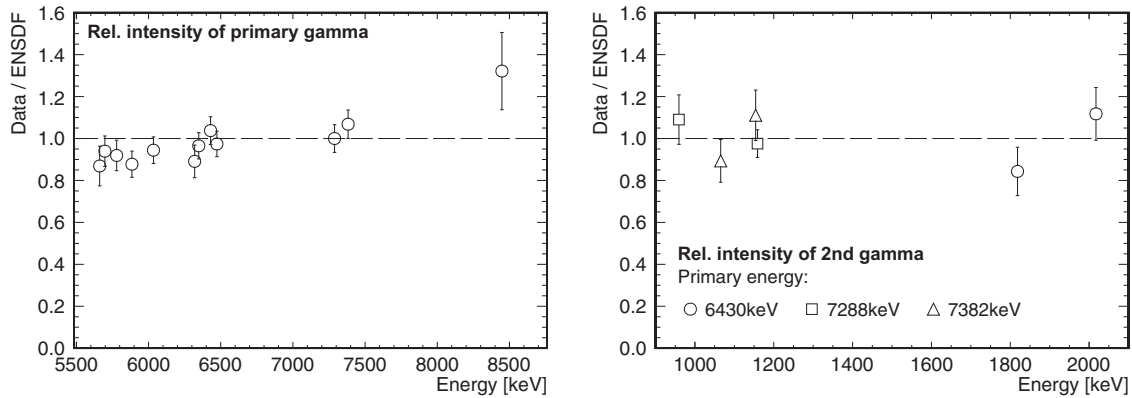


**Fig. 5.** Relative intensity of the primary peaks (left) and the secondary  $\gamma$  rays (right) compared with the values published in *Nuclear Data Sheets* for  $A = 156$  [39].

above 5 MeV as listed in Table 3. The single and double escape peaks were excluded before analyzing these peaks. The direct transition of the resonance state ( $J^\pi = 2^-$ ) to the ground state ( $J^\pi = 0^+$ ) is largely suppressed compared to the transition from 8.536 MeV ( $J^\pi = 2^-$ ) to 0.089 MeV ( $J^\pi = 2^+$ ), emitting a 8.448-MeV  $\gamma$  ray. The tabulated values of the energies are taken from Ref. [39]. In the case of overlapping peaks in our data spectrum, we mention the means of the primary  $\gamma$ -ray energies with their combined intensities. The discrete  $\gamma$ -ray emissions above 5 MeV are expected to arise mostly from the first transition and are hence referred to as “primary”  $\gamma$  rays. By tagging the events with each of these primary  $\gamma$  rays, we obtained the intensities of the secondary  $\gamma$  rays. We found them in fair agreement with the values published in *Nuclear Data Sheets* for  $A = 156$  [39], as displayed in Fig. 5. Details of the comparison methods are described in Ref. [21]. The relative intensities of these discrete peaks add up to  $2.78 \pm 0.02\%$  of the data spectrum.

For the modeling of the continuum part, we compute the probability  $P(E_a, E_b)$  for  $E1$  transitions with  $E_\gamma = E_a - E_b$  in terms of the transmission coefficient  $T_{E1}(E_\gamma)$  and the number of levels  $\rho(E_b)\delta E_b$  as

**Table 3.** List of the 12 discrete peaks from primary  $\gamma$  rays that we identified in our data. The stated energies are taken from Ref. [39], rounded to the nearest keV. In four cases the table lists the unweighted mean energy of known peaks that overlap in our data: (i) 6474 keV, combining 6482 keV and 6466 keV; (ii) 6348 keV, combining 6349 keV and 6345 keV; (iii) 5885 keV, combining 5889 keV and 5884 keV; as well as (iv) 5779 keV, combining 5774 keV and 5786 keV.

	$\gamma$ -ray energy [keV]		Intensity % [ $10^{-2}$ ]
	Primary	Secondary	
1	8448	–	$1.8 \pm 0.2$
2	7382	1154	$12.7 \pm 1.4$
		1065	$10.6 \pm 1.2$
3	7288	1158	$34.8 \pm 2.4$
		959	$10.5 \pm 1.1$
4	6474	1964	$35.2 \pm 0.7$
5	6430	2017	$20.7 \pm 2.2$
		1818	$11.7 \pm 1.5$
		2188	$12.1 \pm 1.7$
6	6348	2097	$9.8 \pm 1.6$
		1154	$4.6 \pm 0.8$
		1065	$3.8 \pm 0.7$
7	6319	2127	$9.4 \pm 0.5$
8	6034	2412	$14.0 \pm 1.7$
		2213	$6.4 \pm 1.0$
9	5885	2563	$9.0 \pm 2.1$
		2364	$8.4 \pm 2.1$
10	5779	2672	$18.8 \pm 0.8$
11	5698	2749	$28.6 \pm 0.8$
12	5661	2786	$15.4 \pm 0.7$

$$P(E_a, E_b) = \frac{dP}{dE}(E_a, E_b) \delta E = \frac{\rho(E_b) T_{E1}(E_\gamma)}{\int_0^{E_a} \rho(E'_b) T_{E1}(E'_\gamma) dE'_b} \delta E, \quad E'_\gamma = E_a - E'_b, \quad (2)$$

where  $\delta E$  is a finite energy step in our computations.  $T_{E1}(E_\gamma)$  refers to the  $E1$  photon strength function  $f_{E1}(E_\gamma)$  (PSF) depending on cross section ( $\sigma_i$ ), the width ( $\Gamma_i$ ), and energy ( $E_i$ ) of the resonances. It is written as

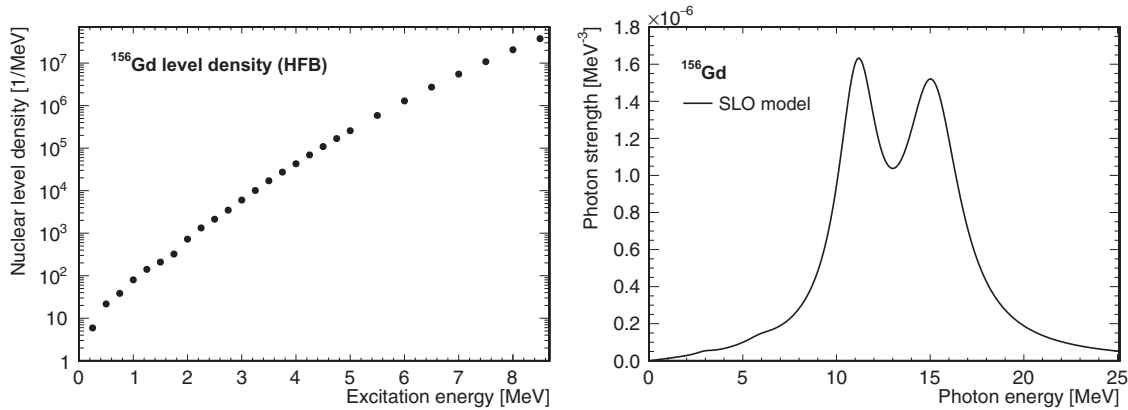
$$T_{E1}(E_\gamma) = 2\pi E_\gamma^3 f_{E1}(E_\gamma), \text{ and} \\ f_{E1}(E_\gamma) = \frac{1}{3(\pi \hbar c)^2} \sum_{i=1}^4 \frac{\sigma_i E_\gamma \Gamma_i^2}{(E_\gamma^2 - E_i^2)^2 + E_\gamma^2 \Gamma_i^2}, \quad (3)$$

where values of  $E_i$ ,  $\sigma_i$ , and width  $\Gamma_i$  are mentioned in Table 4 and  $\rho(E_b)$  is the nuclear level density (NLD). We note that we add two small (pygmy)  $E1$  resonances of the same Lorentzian type ( $i = 3, 4$ ) to the PSF in Eq. (3) in order to check the effect of those two resonances on the  $\gamma$ -ray spectrum [40, 42, 43]<sup>2</sup>, while we used only the first two major  $E1$  resonances in the previous publication [21]. Since

<sup>2</sup> The JENDL-4.0 data file for <sup>155</sup>Gd (Material Number = 6434), evaluated by N. Iwamoto, A. Zukeran, and K. Shibata in 2010, is available; see Ref. [41].

**Table 4.** Parameter values for the PSF of the  $^{156}\text{Gd}$  nucleus [40]. We use the  $E1$  resonances only for our model.

Index $i$	Cross section $\sigma_i$ [mb]	Energy $E_i$ [MeV]	Width $\Gamma_i$ [MeV]
( $E1$ ) 1	242	15.2	3.6
( $E1$ ) 2	180	11.2	2.6
( $E1$ ) 3	2.0	6.0	2.0
( $E1$ ) 4	0.4	3.0	1.0
( $M1$ ) 5	2.03	7.62	4.0
( $E2$ ) 6	3.69	11.7	4.24

**Fig. 6.** Left: Tabulated values [43] for the NLD of  $^{156}\text{Gd}$  from computations based on the HFB method [44,45]. Right: The  $E1$  PSFs for  $^{156}\text{Gd}$ , given as a function of the  $\gamma$ -ray energy, used in the standard Lorentzian model (SLO) approach.

these four resonances are all  $E1$ -type, we can construct probability tables according to Eq. (2) to generate the  $\gamma$ -ray spectrum<sup>3</sup>. The corresponding NLD [43–45] and the PSF [40] used for  $^{156}\text{Gd}$  are shown in Fig. 6 (left and right respectively). Recent reviews on the NLD and the PSF can be found in Refs. [43,46].

#### 4. Final model performance

We first generate the continuum part of the  $\gamma$ -ray spectrum in  $^{156}\text{Gd}$  according to Eq. (2). The result is shown in Fig. 7. We then generate the discrete part according to the relative intensities listed in Table 3 and then compare these two parts with the observed spectrum. We determine the fraction of the discrete part in the total number of events to be  $2.78 \pm 0.02\%$  of the data above 0.11 MeV. The remaining dominant contribution of  $97.22 \pm 0.02\%$  comes from the continuum part of the energy levels in  $^{156}\text{Gd}$ . The continuum and discrete components generated by our MC model are shown separately here for  $^{155}\text{Gd}$ , along with the data in Fig. 8. They are added in the corresponding fractions in Fig. 9 (left). The data spectrum matches our MC spectrum well.

<sup>3</sup> The effect of including the two additional resonances on the gross  $\gamma$ -ray spectrum was not so significant as the case with only the two major  $E1$  resonances. While we add the two  $E1$  resonances ( $i = 3, 4$ ), we do not add the  $M1$  and  $E2$  resonances to the PSF in Eq. (3). If we included the  $M1$  and  $E2$  resonances in Eq. (3), we would have to separate the NLD of Eq. (2) into the NLDs for positive-parity and negative-parity levels; we have not done that in this paper.

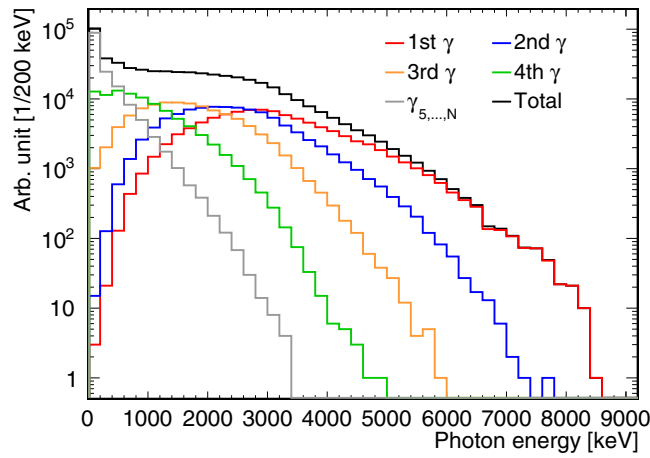


**Fig. 7.** Continuum component (black) according to our model for the  $\gamma$ -ray energy spectrum from the  $^{155}\text{Gd}(n, \gamma)$  reaction and its composition in terms of contributions from the first (red), second (blue), third (orange), fourth (green)  $\gamma$  ray, and other  $\gamma$  rays (gray).

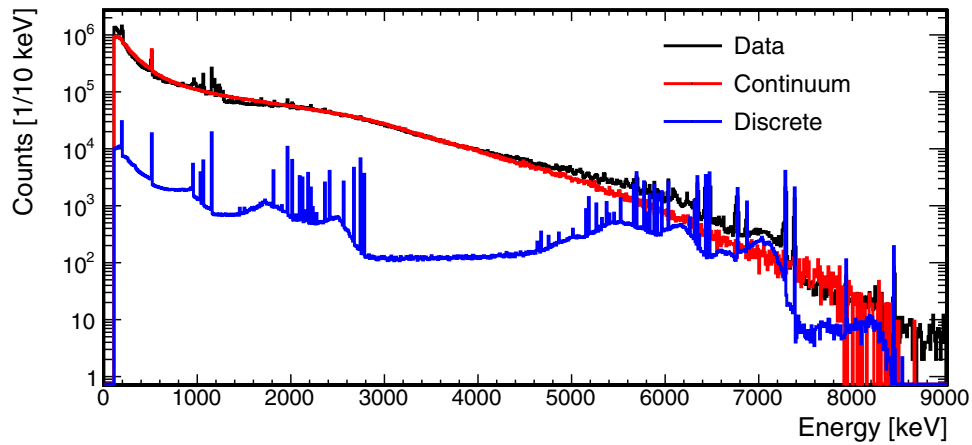


**Fig. 8.** The continuum and discrete components of the spectrum generated by the MC shown separately along with the data spectrum.

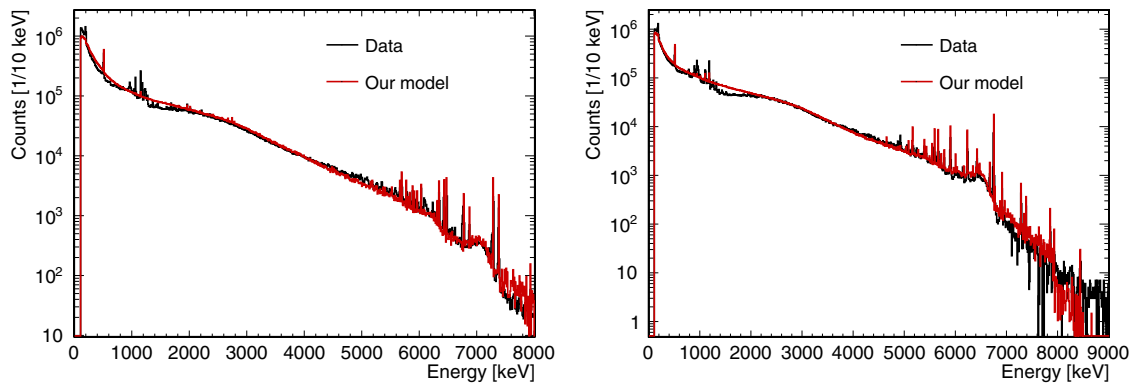


**Fig. 9.** Single energy spectrum (M1H1) generated by our model compared with the data for  $^{155}\text{Gd}$  on the left and  $^{\text{nat}}\text{Gd}$  on the right.

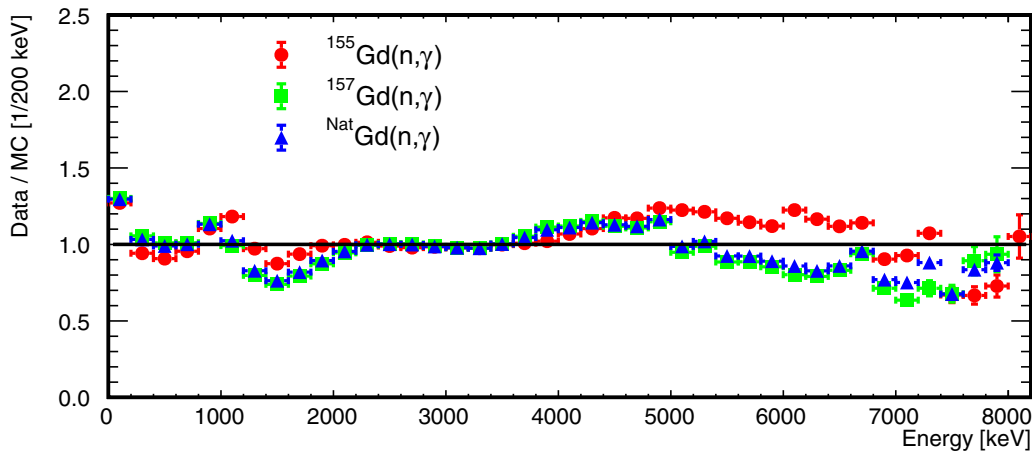


**Fig. 10.** Ratio of data by MC for the single  $\gamma$  events (M1H1 + M1H2) obtained for the  $^{157}\text{Gd}(n, \gamma)$ ,  $^{155}\text{Gd}(n, \gamma)$ , and  $^{\text{nat}}\text{Gd}(n, \gamma)$  cases.

The MC-generated spectrum for  $^{\text{nat}}\text{Gd}(n, \gamma)$  should naturally comprise the spectra for  $^{155}\text{Gd}(n, \gamma)$  and  $^{157}\text{Gd}(n, \gamma)$ , as is obvious with the data spectra in Fig. 4. So, the spectrum for  $^{\text{nat}}\text{Gd}(n, \gamma)$  is obtained by adding the MC spectra generated for  $^{155}\text{Gd}(n, \gamma)$  and  $^{157}\text{Gd}(n, \gamma)$  in the required ratio of their relative cross sections and abundances, as is shown in Fig. 9 (right).

The spectra shown above are single energy spectra (M1H1), which constitute the most dominant ( $\sim 70\%$ ) fraction of the data. In fact, good agreement is found between all the MC-generated spectra and the subsamples of data for different observed multiplicities  $M$ . As examples, the M2H2 and M3H3 spectra are shown in Appendix A.

## 5. Conclusion

The  $\gamma$ -ray spectra generated by our ANNRI-Gd model agree not only with the individual  $^{155}\text{Gd}$  and  $^{157}\text{Gd}$  data set, but also with the  $^{\text{nat}}\text{Gd}$  data set, which are entirely independent<sup>4</sup>. We show the ratio of data/MC in bins of 200 keV for  $^{155}\text{Gd}$ ,  $^{157}\text{Gd}$ , and  $^{\text{nat}}\text{Gd}$  in Fig. 10, for the single  $\gamma$ -ray  $M = 1$  events as an approximate representation of the goodness of our model. For the presented single  $\gamma$ -ray spectrum with the 200 keV binning, the mean deviation of the single ratios from the mean ratio is about 17% for each of  $^{157}\text{Gd}$ ,  $^{155}\text{Gd}$ , and  $^{\text{nat}}\text{Gd}$  spectra. The same ratios for the  $M = 2$  and  $M = 3$  samples are shown in Fig. A.4. They are all in good agreement at a similar level to those published for the  $^{157}\text{Gd}(n, \gamma)$  reaction [21]. With this article, we have completed a consistent model (the ANNRI-Gd model) to generate the gross spectrum for the thermal  $^{155}\text{Gd}$ ,  $^{157}\text{Gd}$ , and  $^{\text{nat}}\text{Gd}(n, \gamma)$  reaction.

In comparison, the more sophisticated model [35] tries to include a small contribution of the  $M1$  (scissors mode) or  $E2$  resonance around 3 MeV in the PSF in order to explain the energy spectra in the sample of two-step cascade  $\gamma$  rays from the thermal neutron capture reactions. The DANCE experiment [28,29] also suggested a need for small resonances ( $M1$  or  $E2$ ) around 3 MeV in addition

<sup>4</sup> The data of  $^{155}\text{Gd}$  and  $^{157}\text{Gd}$  were used to tune the discrete part of our MC model, while the  $^{\text{nat}}\text{Gd}$  data was untouched during the building of our MC.

to the major  $E1$  PSFs in order to explain the  $\gamma$ -ray energy spectra of the multiplicity  $M = 2$ , though the data of the  $^{155,157}\text{Gd}(n, \gamma)$  reactions were taken in neutron kinetic energies in values of tens of eV. To further refine the present modeling, we intend to work on a sample of  $2\gamma$  rays including strong discrete cascade transitions. We note that those samples constitute a few % of the total number of capture events. As these previous articles point out, we must handle the positive-parity states and negative-parity states separately in the NLD or in any discrete levels in order to take into account the  $E1$  transition or  $M1/E2$  transition correctly during the cascade.

After we submitted this article in August 2019, the Daya Bay Collaboration, one of the most advanced reactor-neutrino experiments, reported a Monte Carlo study of the  $\gamma$ -ray spectra from the thermal neutron capture on  $^{155}\text{Gd}$  and  $^{157}\text{Gd}$  and showed large discrepancies in the  $\gamma$ -ray spectra generated by various Monte Carlo models [47]. We compare our spectrum with their result in Appendix B. It shows clearly that our data and our MC model will help resolve such discrepancies in the gross  $\gamma$ -ray spectrum generated by various MC models for the thermal  $^{155}\text{Gd}$ ,  $^{157}\text{Gd}$ , and  $^{\text{nat}}\text{Gd}(n, \gamma)$  reactions.

### Acknowledgements

This work is supported by a JSPS Grant-in-Aid for Scientific Research on Innovative Areas (Research in a proposed research area) No. 26104006 and No. 15K21747. It benefited from the use of the neutron beam of the JSNS and the ANNRI detector at the Material and Life Science Experimental Facility of the Japan Proton Accelerator Research Complex.

### Appendix A. Double/triple $\gamma$ -ray spectra

Apart from the single  $\gamma$ -ray events ( $M = 1$ ), the  $M = 2$  and  $M = 3$   $\gamma$ -ray events are also observed. The M1H1 sample is the most dominant one, followed by the M1H2 sample. Our model agrees with the data in both cases. The relative fractions (in %) in the data and MC for the different subsamples (M1H1, M1H2, M2H2, etc.) are shown in Fig. A.1. Data and MC agree well. The corresponding spectra for the M2H2 and M3H3 samples generated by our model also agree well with the  $^{155}\text{Gd}(n, \gamma)$  and the  $^{\text{nat}}\text{Gd}(n, \gamma)$  data, as shown in Figs. A.2 and A.3, respectively. The ratios of data/MC are also shown in Fig. A.4.

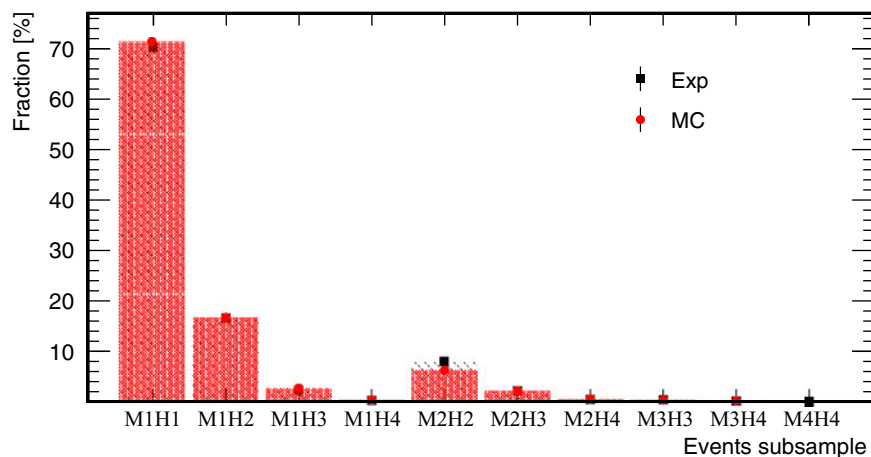


**Fig.A.1.** Relative fraction in % in the data and MC for the different subsamples: M1H1, M1H2, M2H2, etc.

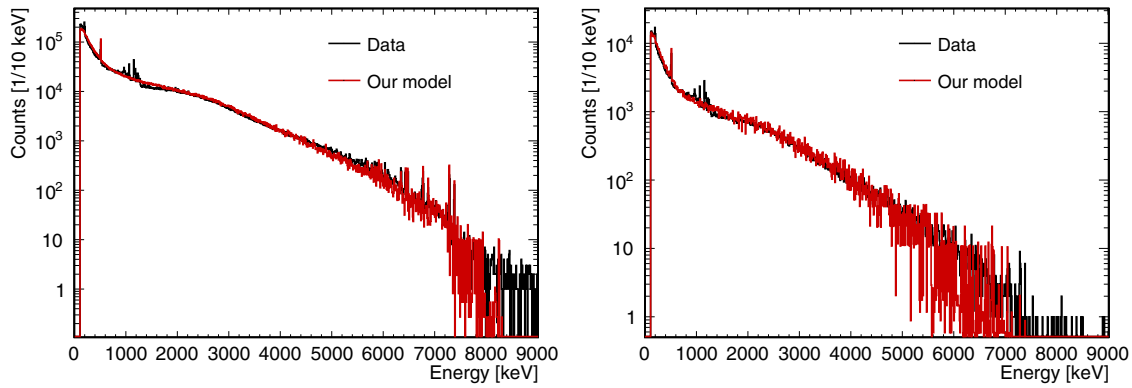


**Fig.A.2.** The  $^{155}\text{Gd}(n, \gamma)$  spectra for M2H2 (left) and M3H3 (right) samples from data and our model MC.

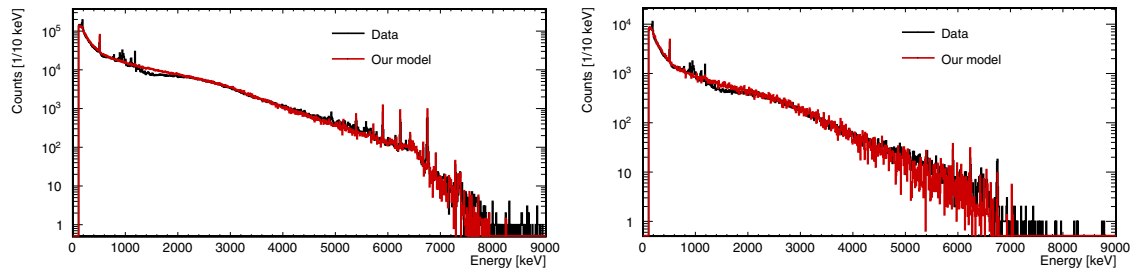


**Fig.A.3.** The  $^{\text{nat}}\text{Gd}(n, \gamma)$  spectra for M2H2 (left) and M3H3 (right) samples from data and our model MC.

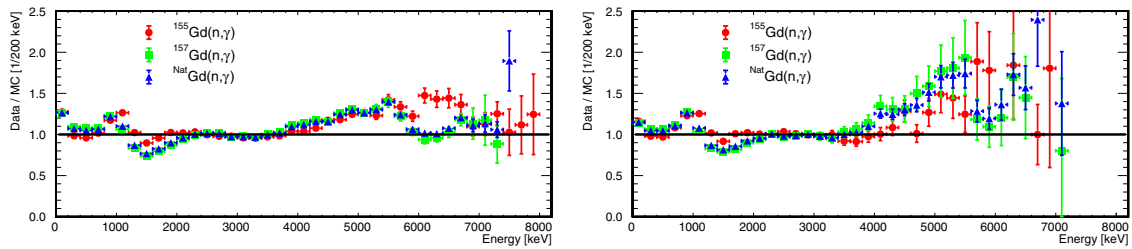


**Fig.A.4.** Ratios of data/MC for M2H2 (left) and M3H3 (right) samples obtained for the  $^{157}\text{Gd}(n, \gamma)$ ,  $^{155}\text{Gd}(n, \gamma)$ , and  $^{\text{nat}}\text{Gd}(n, \gamma)$  cases.

## Appendix B. Comparison of the ANNRI-Gd model with various models reported by the Daya Bay Collaboration

Recently, the Daya Bay Collaboration showed  $\gamma$ -ray spectra of the thermal neutron capture on  $^{155}\text{Gd}$  and  $^{157}\text{Gd}$  in Figs. 5(a) and (b) of Ref. [47], produced by various MC models. We use their Fig. 5(a), which they quote as the energy distribution of the de-excitation gammas of  $^{155}\text{Gd}$ . We add to their Fig. 5(a) a single  $\gamma$ -ray spectrum (purple line) as shown in Fig. B.1, which is generated by our ANNRI-Gd model. We note that we are comparing the shape among various models and that we normalize the histogram by the total entries in the figure<sup>5</sup>. We have already shown in Figs. 4 and 10 that our predictions agree with our measured spectra within about 17% at 200 keV binning. Our model agrees well with Model 1 (a native Geant4 model) for  $E_\gamma$  above 2 MeV, but our model

<sup>5</sup> We read the entries off the histogram of Fig. 5(a) of Ref. [47] and generated Fig. B.1. Thus, the values of the histogram may be different from the original values by a few %.

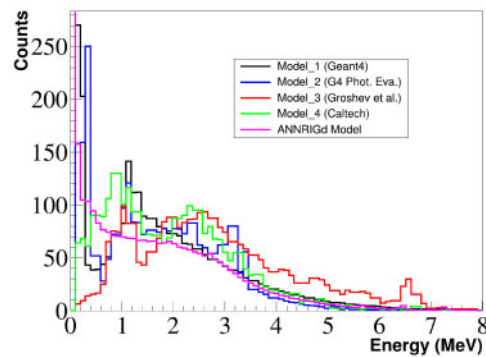


**Fig. B.1.** Energy distribution of  $\gamma$  rays from the  $^{155}\text{Gd}(n, \gamma)$  reaction for Models 1–4 shown in Ref. [47] and our ANNRI-Gd model prediction (purple line).

disagrees with Model 1 below 2 MeV. Other models generate spectra that are very different from ours in shape. We would like to stress again that we can discuss small structures at 2–3 MeV such as the scissors mode only after we understand the gross spectrum over the entire energy region.

## References

- [1] S. F. Mughabghab, *Atlas of Neutron Resonances, Fifth Edition: Resonance Parameters and Thermal Cross Sections, Z = 1–100* (Elsevier, Amsterdam, 2006).
- [2] G. Leinweber, D. P. Barry, M. J. Trbovich, J. A. Burke, N. J. Drindak, H. D. Knox, R. V. Ballad, R. C. Block, Y. Danon, and L. I. Severnyak, *Nucl. Sci. Eng.* **154**, 261 (2006).
- [3] H. D. Choi et al., *Nucl. Sci. Eng.* **177**, 219 (2014).
- [4] M. Mastromarco et al. [n\_TOF Collaboration], *Eur. Phys. J. A* **55**, 9 (2019).
- [5] Y. Abe et al. [Double Chooz Collaboration], *Phys. Rev. Lett.* **108**, 131801 (2012).
- [6] J. K. Ahn et al. [RENO Collaboration], *Phys. Rev. Lett.* **108**, 191802 (2012).
- [7] F. P. An et al. [Daya Bay Collaboration], *Phys. Rev. Lett.* **108**, 171803 (2012).
- [8] Y. J. Ko et al. [NEOS Collaboration], *Phys. Rev. Lett.* **118**, 121802 (2017).
- [9] H. Almazán et al. [STEREO Collaboration], *Phys. Rev. Lett.* **121**, 161801 (2018).
- [10] H. Almazán et al. [STEREO Collaboration], *Eur. Phys. J. A* **55**, 183 (2019).
- [11] I. Alekseev et al. [DANSS Collaboration], *Phys. Lett. B* **787**, 56 (2018).
- [12] A. P. Serebrov et al. [Neutrino-4 Collaboration], *JETP Lett.* **109**, 213 (2019).
- [13] M. Harada et al. [JSNS<sup>2</sup> Collaboration], [arXiv:1610.08186](https://arxiv.org/abs/1610.08186) [physics.ins-det] [[Search INSPIRE](#)].
- [14] S. Oguri, Y. Kuroda, Y. Kato, R. Nakata, Y. Inoue, C. Ito, and M. Minowa, *Nucl. Instrum. Meth. A* **757**, 33 (2014).
- [15] J. F. Beacom and M. R. Vagins, *Phys. Rev. Lett.* **93**, 171101 (2004).
- [16] H. Sekiya [for Super-Kamiokande Collaboration], *PoS ICHEP2016*, 982 (2016).
- [17] H. Watanabe et al. [Super-Kamiokande Collaboration], *Astropart. Phys.* **31**, 320 (2009).
- [18] K. Pushkin et al. [LZ Collaboration], *Nucl. Instrum. Meth. A* **936**, 162 (2019).
- [19] S. Moriyama [for XENONnT Collaboration], Direct Dark Matter Search with XENONnT, a talk Presented at The International Symposium on Revealing the history of the Universe with Underground Particle and Nuclear Research, March 8, 2019, Tohoku University.
- [20] K. J. R. Rosman and P. D. P. Taylor, *Pure Appl. Chem.* **70**, 217 (1998).
- [21] K. Hagiwara et al. [ANNRI-Gd Collaboration], *Prog. Theor. Exp. Phys.* **2019**, 023D01 (2019).
- [22] M. Igashira, Y. Kiyonagi, and M. Oshima, *Nucl. Instrum. Meth. A* **600**, 332 (2009).
- [23] A. Kimura et al., *J. Nucl. Sci. Technol.* **49**, 708 (2012).
- [24] T. Kin et al., *J. Korean Phys. Soc.* **59**, 1769 (2011).
- [25] K. Kino et al., *Nucl. Instrum. Meth. A* **626**, 58 (2011).
- [26] K. Kino et al., *Nucl. Instrum. Meth. A* **736**, 66 (2014).
- [27] S. Nagamiya, *Prog. Theor. Exp. Phys.* **2012**, 02B001 (2012).
- [28] B. Baramsai et al. [DANCE Collaboration], *Phys. Rev. C* **87**, 044609 (2013).

- [29] A. Chyzh et al. [DANCE Collaboration], Phys. Rev. C **84**, 014306 (2011).
- [30] J. Kroll et al., Phys. Rev. C **88**, 034317 (2013).
- [31] F. Bečvář, Nucl. Instrum. Meth. A **417**, 434 (1998).
- [32] L. V. Groshev, A. M. Demidov, V. N. Lutsenko, and V. I. Pelekhov, J. Nucl. Energy **9**, 50 (1959).
- [33] L. V. Groshev, A. M. Demidov, V. A. Ivanov, V. N. Lutsenko, and V. I. Pelekhov, Bull. Acad. Sci. USSR **26**, 1127 (1963).
- [34] L. V. Groshev, A. M. Demidov, V. I. Pelekhov, L. L. Sokolovskii, G. A. Bartholomew, A. Doveika, K. M. Eastwood, and S. Monaro, Nucl. Data Tables A **5**, 1 (1968).
- [35] S. Valenta, F. Bečvář, J. Kroll, M. Krtička, and I. Tomandl, Phys. Rev. C **92**, 064321 (2015).
- [36] S. Agostinelli et al. [Geant4 Collaboration], Nucl. Instrum. Meth. A **506**, 250 (2003).
- [37] J. Allison et al. [Geant4 Collaboration], IEEE Trans. Nucl. Sci. **53**, 270 (2006).
- [38] G. Harton-Smith et al., *GLG4sim: Generic liquid-scintillator anti-neutrino detector Geant4 simulation* (2005) (available at: <https://www.phys.ksu.edu/personal/gahs/GLG4sim/>, date last accessed February 5, 2019).
- [39] C. W. Reich, Nucl. Data Sheets, **113**, 2537 (2012).
- [40] K. Shibata et al., J. Nucl. Sci. Technol. **48**, 1 (2011).
- [41] (available at: <https://www.ndc.jaea.go.jp/jendl/j40/j40f64.html>).
- [42] J. Kopecky and M. Uhl, Phys. Rev. C **41**, 1941 (1990).
- [43] R. Capote et al. [RIPL-3], Nucl. Data Sheets **110**, 3107 (2009).
- [44] S. Goriely, M. Samyn, and J. M. Pearson, Phys. Rev. C **75**, 064312 (2007).
- [45] S. Goriely, S. Hilaire, and A. J. Koning, Phys. Rev. C **78**, 064307 (2008).
- [46] S. Goriely et al., Eur. Phys. J. A **55**, 172 (2019).
- [47] D. Adey et al. [Daya Bay Collaboration], Phys. Rev. D **100**, 052004 (2019).